EVALUATING INTERFACIAL CHARGE TRANSFER KINETICS AND ENERGETICS VIA LASER BASED SPECTROELECTROCHEMICAL METHODS

Susan G. Yan and Joseph T. Hupp
Dept. of Chemistry and Materials Research Center
Northwestern University
2145 Sheridan Road
Evanston, IL 60208

Laser based electroanalytical methods can be used to determine: a) rates for fast interfacial electron transfer, b) conduction band edge energies for metal-oxide semiconductors, and c) approximate redox potentials of short lived molecular photo excited states. Case studies involving ML_3^{n-} species and titanium dioxide electrodes reveal unusual reaction rate/driving force effects that are seemingly inconsistent with simple interfacial electron transfer schemes, but are accommodated by a combined electron transfer/proton transfer sequence.

INTRODUCTION

The marriage of electrochemistry and laser spectroscopy under the guise of SERS (1), conventional resonance Raman scattering (2), second harmonic generation (3,4), surface activation (5), ultrafast luminescence (6), fluorescence electrochromism (7), T-jump kinetics (8), pump/probe kinetics (9,10) and numerous other strategies has been tremendously prosperous. The combined methodologies have yielded information of unprecedented depth regarding interfacial energetics and structure, molecular vibrational structure and charge transfer reactivity. In this paper we illustrate some of these applications via a case study of fast interfacial electron transfer (ET) at titanium dioxide semiconductor/solution interfaces. The problems examined are: 1) rapid initiation and subsequent assessment of kinetics for interfacial ET reactions, 2) energetics of the semiconductor/solution interface, and 3) approximate energetics of molecular photo excited states. Also discussed is the significance of the results in the context of current discussions of *mechanisms* of charge transfer at semiconductor/solution interfaces.

EXPERIMENTAL SECTION

Materials. Colloidal titanium dioxide was prepared by a variant of the method of O'Regan, et al. (11). Briefly, 2.6 ml of concentrated HNO_3 was combined with 375 ml of deionized water. 30 ml of $Ti(OCH(CH_3)_2)_4$ (Aldrich) was then added dropwise to the stirring solution over a period of 2 minutes. The solution was then stirred for 3 days at room

temperature. High resolution transmission electron microscopy revealed that the resulting colloidal solution was comprised of nanocrystalline particles of 5 nm average diameter. Electron diffraction measurements (Figure 1) establish that particles prepared in this fashion are anatase rather than rutile.

High area semiconductor films were prepared by the method of O'Regan and Grätzel (12). (We thank Prof. Nate Lewis and Dr. S. Doig for providing us with a detailed description of this method.) Briefly, these materials were prepared as described above, except that the initial hydrolysis product was stirred for 2 hours at room temperature and then for 8 hours at 80°C to evaporate the propanol formed. The resulting sol was heated for an additional 12 hours at 200° C in a stainless steel pressure vessel. Water was then removed by rotary evaporation until a sol concentration of 160 g/l was achieved. Carbowax 20,000 (40% weight equivalent of TiO_2) was added to the concentrated sol and the mixture was stirred overnight. Films were prepared by spin coating the sol on conductive glass (fluorine-doped tin oxide) and then annealing the assembly for 1 hour in air at 400° C.

RuL_3^{10-} (L = 4,4'-$(CH_2PO_3)_2$-2,2'-bipyridine) was prepared from $RuCl_3$ and 4,4'-$(CH_2PO(OCH_2CH_3)_2)_2$-2,2'-bipyridine as previously described (13). OsL_3^{10-} was prepared in a similar fashion, except that the reaction time was extended to 3 days from 3 hours and ammonium hexachloroosmate was used in place of the metal trichloride. Unfortunately, the osmium compound proved insufficiently soluble to characterize fully by the time of the symposium. Further characterization is being attempted; however, in view of the incomplete characterization, the results described here must necessarily be viewed as preliminary.

Measurements. Rates for interfacial electron transfer were measured by a pump/probe technique based on Q-switched laser excitation, as previously described (13). Diode laser reflectance measurements were performed as described by Lyon (14). Except as noted, electrochemical and photochemical measurements were made in water at pH = 2.5. Potentials are reported versus a saturated (NaCl) calomel electrode (s.s.c.e.).

RESULTS

Systems. The reactions examined were electron transfer from titanium dioxide to $Os^{III}L_3^{9-}$ and $Ru^{III}L_3^{9-}$ where the methylphosphonate functionalities on the bipyridine ligands, L, serve to anchor the molecules to the semiconductor surface (13, 15). (Preliminary results for the ruthenium reactant have recently been reported elsewhere (13).) Comparison of the pair of molecules is of interest, in part, because their formal reduction potentials ($M^{III/II}$ couples) differ by roughly 400 mV. This implies that the energetics of electron transfer will be substantially different for the two reactions – where, surprisingly, the precise role of energetics has yet to be established clearly for these types of reactions. The reactants are also of interest because of their ability, in oxidation state II, to collect substantial portions of the solar spectrum (9-13, 16) and to serve, therefore, as sensitizers in semiconductor based photovoltaic cells.

Scheme I. Electron-Injection and Back Electron Transfer

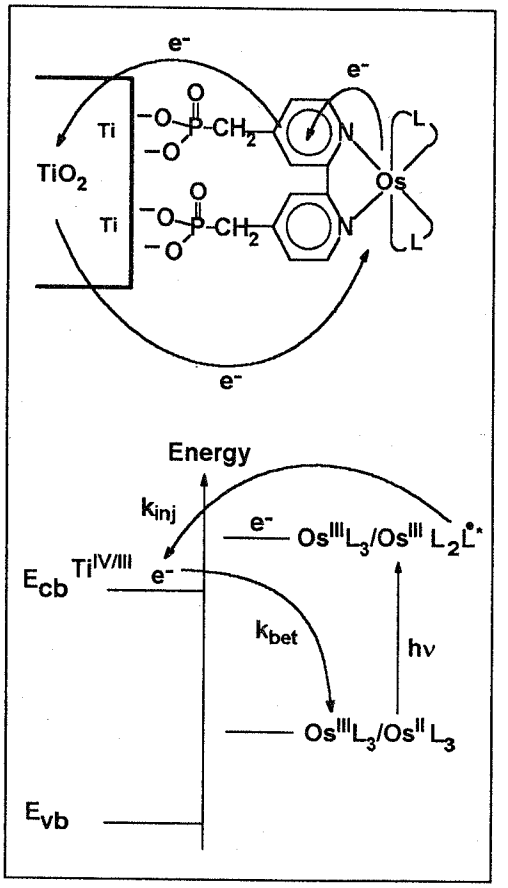

Kinetics. As indicated in Scheme I, the reaction sequence is initiated by photo exciting the surface-attached metal complexes. The excited state is highly reducing and is capable of transferring an electron rapidly to the conduction band or other states of the semiconductor. In the absence of other reactions, the injected electron can return to the metal complex via interfacial charge transfer. To follow this sequence temporally, we used a frequency-doubled (532 nm), Q-switched Nd:YAG laser (~3 ns pulse width) as a pump beam and a pulsed Xenon lamp as a probe beam. In each case, the feature monitored was a metal-to-ligand charge transfer band. This feature exists in the ground state, but is absent in both the photo excited state and the oxidized state. As shown in figure 2 for complexes bound to high area TiO_2 electrodes, the injection processes occur within the rise time of the excitation pulse. The back electron transfer processes, signified by the recoveries of the bleached absorbances, are slower and are distinctly biphasic. We have shown elsewhere for the ruthenium reactant that the longer component of the transient absorbance signal can be selectively and reversibly eliminated by biasing the semiconductor (in thin film form) just positive of the potential of the conduction band edge. As shown in figure 3, the osmium reactant behaves similarly. A tentative interpretation for this effect (figure 4) is that biasing fills mid-gap states thereby preventing injection and precluding back electron transfer. Regardless of the detailed chemical explanation, the apparent electrical separability of the absorbance recovery processes lends credibility to the idea of kinetic separability. With this in mind, we modeled the reaction kinetics as an approximately biexponential recovery process where the time constant for the second exponential was sufficiently large for the osmium reactant such that the corresponding recovery term could be treated (over short times, t) as a constant:

$$[(A(t) - A_\infty)/(A_o - A_\infty)] = a\bullet[1 - \exp(-k_{bet}\, t)] + b\bullet[1 - \exp(-k'_{bet} t)] + \text{constant} \quad (1)$$

Shown as smooth lines in figure 2 are best fits to eq. 1 for data collected in the 0 to 500 ns (Ru) or 1,000 ns (Os) time range. (For analyses over a wider time window, Ford and Rodgers have shown that absorbance transients are better described by a stretched exponential

recovery, where the stretched exponential may be indicative of distributed kinetics for the slower recovery process (17).) In any case, given the electrochemical effects and the likely kinetic complexity of the slower recovery process, we will focus our attention on the faster process described by k_{bet}. For RuL_3^{n-}, k_{bet} is 3.1 x 10^7 s^{-1}, in reasonable agreement with the rate constant obtained previously with titanium dioxide electrodes prepared from Degussa P25 (a mixed anatase/rutile material). For OsL_3^{n-}, k_{bet} on high area anatase electrodes is 1.6 x 10^7 s^{-1}. Extension of the measurements to pH = -4.1 and pH = +7.0 yielded rate constants of 1.6 x 10^7 s^{-1} and 1.5 x 10^7 s^{-1}, respectively. (Similar pH-independent reactivity has been noted previously for RuL_3^{n-} (13).) For reactions on colloidal TiO_2 the rate constants are slightly smaller, but a reactivity advantage for ruthenium over osmium is still encountered (i.e. $k_{bet}(Ru)$ = 2.5 x 10^7 s^{-1}; $k_{bet}(Os)$ = 0.7 x 10^7 s^{-1}).

Energetics. Scheme I provides a framework for discussing energetics. From the diagram, an understanding of the electron injection process requires a knowledge of the relative energies of the conduction band or other electron accepting sites and the pertinent molecular excited states. We have shown previously (14) that near infrared (786 nm) laser reflectance measurements can be used to estimate conduction band edge energies, E_{CB}. The experiment relies upon attenuation of reflected light at electrode potentials more negative than E_{CB}, where the attenuation effect arises because near infrared light can be absorbed by conduction band electrons accumulated at the interface. Figure 5 shows typical reflectance versus potential curves for a nanocrystalline titanium dioxide film with and without surface-bound RuL_3^{n-}. Also illustrated in the figure (inset) is the well known Nernstian dependence of E_{CB} upon pH, observed here via the reflectance technique.

Molecular excited state redox potentials usually are estimated by combining ground state potentials with emission energies (18). Unfortunately, both RuL_3^{10-} and OsL_3^{10-} are nonemissive when immobilized on titanium dioxide surfaces. We reasoned, however, that approximate measures of excited state oxidation potentials (ML_3^{10-*}/ML_3^{9-}) could be obtained via a transient absorbance experiment in which acceptor levels on the electrode surface are progressively filled by adjusting the electrode potential in the negative direction. The injection process should be stymied at the point where all semiconductor acceptor levels at or below the energy of the molecular excited state are occupied, i.e. where the reaction is no longer exergonic. The approach relies, therefore, on the availability of a range of mid-gap states capable of receiving electrons from a surface bound reactant. (Note that the availability of such states has already been established above (Figure 3) via transient absorbance studies.)

To extend the voltage range over which relevant mid-gap states could be accessed, we replaced water with acetonitrile as solvent. Under dry conditions, with tetrabutylammonium perchlorate as electrolyte, Redmond and Fitzmaurice have reported that the conduction band edge can be shifted as far negative as -2.04 V vs. s.c.e. (19). With the reflectance technique, we find that E_{CB} in acetonitrile (with tetraethylammonium perchlorate) is ca. -1.6 V vs. s.s.c.e.. ("Conditioning" of the electrode via repetitive potential cycling eventually shifts the onset potential for reflectance attenuation to a value close to that reported by Redmond and Fitzmaurice (19).) Evaluation of the excited state electron injection process in acetonitrile yields the results shown in figure 6 where the relative magnitudes of

transient absorbance signals are plotted versus the externally applied potential. For both reactants, the plots are sigmoidal with interfacial ET apparently completely eliminated at potentials more negative than -1.05 V. We suggest that the midpoints of these curves (ca. -0.9 V for both) can be taken as approximate measures of formal potentials for the ML_3^{10-*}/ML_3^{11-} couples. The similarity in estimated reduction potentials for the two photo reactants was expected and is consistent with the shared bipyridine radical anion nature of the reactive excited states. Interestingly, the estimated potentials are close to those reported for the parent 2,2'-bipyridine ruthenium compound in solution (20).

For the back electron transfer reaction (Scheme I), the relevant energetics are those for the electron in the electrode and for the ground state $M^{III}L_3^{9-}/M^{II}L_3^{10-}$ couple. Ideally the latter should be determined for the couple in its surface-bound state. In principle, this can be accomplished via direct voltammetry measurements on a dark electrode if a sufficient number of mid-gap states exists in the vicinity of the reactant's formal potential. Indeed, this strategy has been successfully implemented by Meyer and co-workers for similar reactants on nanocrystalline TiO_2 surfaces (21). Unfortunately, our electrodes exhibited insulating behavior in the desired potential range. Potentials were estimated, therefore, from cyclic voltammograms for partially hydrolyzed ML_3^{n-} complexes in acetonitrile as solvent. The values obtained were +0.83 V and +1.24 V for Os(III/II) and Ru(III/II), respectively.

DISCUSSION

Figures 2 and 3 illustrate that fast interfacial electron transfer reactions that would be difficult to monitor kinetically by conventional electrochemical methods are relatively easily followed by transient absorbance techniques. Laser based measurements also can provide information about electrode energetics (E_{CB}, figure 5) and approximate energetics of nonluminescent molecular excited states (figure 6).

The combination of kinetics and energetics data raises some interesting fundamental questions concerning mechanisms of electron transfer at metal-oxide semiconductor/solution interfaces. The conventional wisdom is that forward ET occurs by energetically optimized electron injection into the conduction band and that back ET occurs with inverted energetics (22). The reverse ET process has sometimes been treated theoretically by assuming that high frequency vibrational modes define the pertinent Franck-Condon factors (23) and that radiationless decay theory can be employed (24). For metal centered reductions of ML_3^{n-} species, however, the relevant Franck-Condon factors are almost certainly those associated with classical solvent modes (25), low frequency metal-ligand stretching modes and/or low and intermediate frequency electrode lattice modes (26). Consequently, classical Marcus theory (27) (or equivalently, the high temperature limit of radiationless decay theory (24, 28)) should apply.

Figure 7 shows a hypothetical Marcus rate plot for a classical reaction featuring a 1 eV reorganization energy (a reasonable upper limit for $Os^{III}L_3^{9-}$ or $Ru^{III}L_3^{9-}$ reduction) and an arbitrary pre-exponential factor of 10^{12} s^{-1} (i.e., an essentially adiabatic reaction). The absolute magnitudes of rate constants calculated in this way are without particular significance. The calculated trends, however, are meaningful. To illustrate, points corresponding to the

reduction of $Ru^{III}L_3^{9-}$ (pH = 2.5) and $Os^{III}L_3^{9-}$ (pH = -4.1, 2.5 and 7.0) by electrons at the bottom of the conduction band of titanium dioxide are labeled. (Driving forces are equated with the difference between E_{CB} and the formal potential for reduction of $M^{III}L_3^{9-}$.) From the figure, classical Marcus theory predicts: a) enormous increases in k_{bet} with decreasing pH, and b) large increases in k_{bet} upon replacement of ruthenium by osmium. Instead, we observe an essentially complete lack of dependence of k_{bet} upon pH, and a modest *decrease* in reactivity upon replacement of ruthenium by osmium. The reaction kinetics clearly are decoupled from whatever energetic factors determine the pH dependence of E_{CB}. The experimental results also point to Marcus normal region (left hand side of figure 7) rather than inverted region reactivity (right hand side of figure 7), despite the large driving forces.

To account for the anomalous driving force effects, we turn to recent electrochemical quartz crystal microbalance studies which show that addition of electrons to the conduction band of titanium dioxide is accompanied quantitatively by the intercalation of charge compensating cations from the electrolyte solution (14). In aqueous solutions, the intercalated ion is the proton. In the limit of highly localized electron addition, the addition process can be viewed as reduction of surface or near surface Ti^{IV} to Ti^{III}. Furthermore, the potential for the onset of this process can be equated with E_{CB}. Inclusion of proton intercalation then leads to eq. 1 and provides a "Pourbaix" type explanation for the well known dependence of E_{CB} on pH.

$$Ti^{IV}O_2 + e^- + H^+ \rightarrow Ti^{III}O(OH) \qquad (2)$$

If eq. 2 is applicable, then driving forces obtained from the difference between E_{CB} and the potential for reduction of $M^{III}L_3^{9-}$ will describe a combined electron and proton transfer reaction, rather than a pure electron transfer reaction:

$$Ti^{III}O(OH) + M^{III}L_3^{9-} \rightarrow Ti^{IV}O_2 + M^{II}L_3^{10-} + H^+(solution) \qquad (3)$$

If the electron transfer and proton transfer occur in mechanistically distinct steps, then the *kinetically* relevant driving forces (e.g., those used in Marcus theory) will be the free energy changes for the isolated steps, rather than the overall reaction. Scheme II shows a possible reaction sequence for electron injection and back ET. If reaction 7 is rate determining, then the back ET process will be pH independent despite pH-induced shifts in E_{CB}. Furthermore, the driving force for eq. 7 will be substantially less than the measured driving force for the overall back reaction (eq. 3 (eqs. 7 +8)). If the driving force attenuation is great enough, then the isolated back ET step will occur in the Marcus normal region rather than the inverted region and k_{bet}(Ru) will exceed k_{bet}(Os), as indeed observed experimentally.

Scheme II

$$Ti^{IV}O_2 + M^{II}L_3^{10-} \rightarrow Ti^{IV}O_2 + ML_3^{10-*} \quad (4)$$

$$Ti^{IV}O_2 + ML_3^{10-*} \rightarrow Ti^{III}O_2 + M^{III}L_3^{9-} \quad (5)$$

$$Ti^{III}O_2 + M^{III}L_3^{9-} + H^+(solution) \rightarrow Ti^{III}O(OH) + M^{III}L_3^{9-} \quad (6)$$

$$Ti^{III}O(OH) + M^{III}L_3^{9-} \rightarrow Ti^{IV}O(OH) + M^{II}L_3^{10-} \quad (7)$$

$$Ti^{IV}O(OH) + M^{II}L_3^{10-} \rightarrow Ti^{IV}O_2 + M^{II}L_3^{10-} + H^+(solution) \quad (8)$$

Scheme II is admittedly speculative. We have obtained supporting evidence, however, from photo intercalation experiments (29) and additional molecule-based driving force studies to be described elsewhere (30). Further support for the hypothesis could be provided by variable temperature experiments, if it could be shown that back ET is thermally activated and that the activation barrier for $Os^{III}L_3^{9-}$ reduction exceeds that for $Ru^{III}L_3^{9-}$ reduction.

CONCLUSIONS

Laser based electroanalytical methods can be used to determine: a) rates for fast interfacial electron transfer, b) conduction band edge energies for metal-oxide semiconductors, and c) approximate redox potentials of short lived molecular photo excited states. Case studies involving ML_3^{n-} species and titanium dioxide electrodes reveal unusual reaction rate/driving force effects that are seemingly inconsistent with simple interfacial electron transfer schemes, but are accommodated by a combined electron transfer/proton transfer sequence.

REFERENCES

1. D. L. Jeanmaire and R. P. Van Duyne, J. Electroanal. Chem., **84**, 1 (1977).
2. D. L. Jeanmaire, M. R. Suchanski and R. P. Van Duyne, J. Am. Chem. Soc., **97**, 1699 (1975).
3. R. M. Corn and D. A. Higgins, Chem. Rev., **94**, 107 (1994).
4. P. R. Fischer, J. L. Daschbach, D. E. Gragson and G. L. Richmond, J. Vac. Sci. Technol., A, **12**, 2617 (1994).

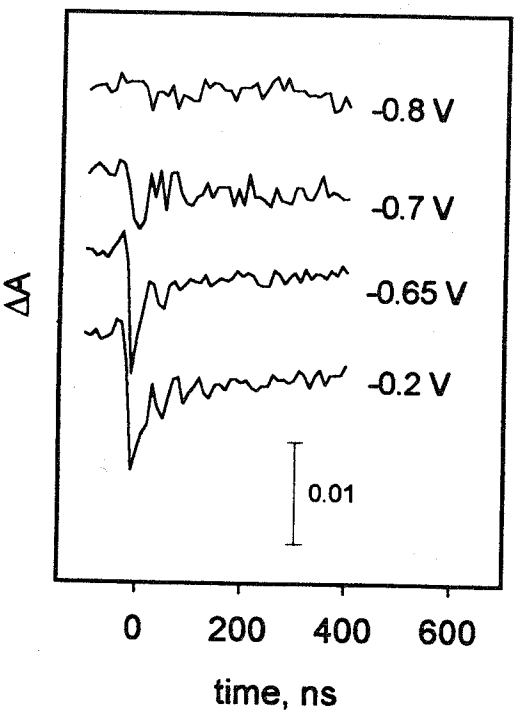

Figure 3. Potential dependence of transient absorbance signals for OsL_3^{n-} on TiO_2 in contact with water at pH 2.5. λ_{pump} = 532 nm. λ_{probe} = 464 nm. For clarity, curves are offset along absorbance axis.

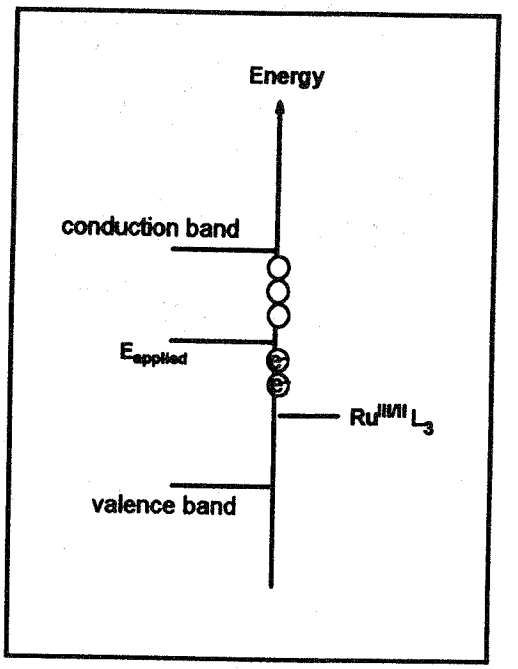

Figure 4. Schematic representation of partial filling of mid-gap states. Note that higher energy corresponds to more negative applied potential. (In view of the small particle size, band bending effects are omitted from the diagram.)

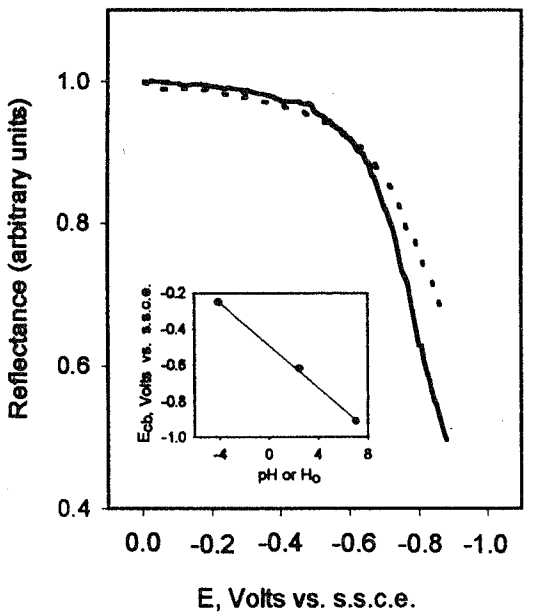

Figure 5. Diode laser reflectance vs. applied potential for nanocrystalline TiO_2 with (dashed line) and without (solid line) attached RuL_3^{10-} at pH 2.5. Inset: pH dependence of E_{CB} measured by electroreflectance.

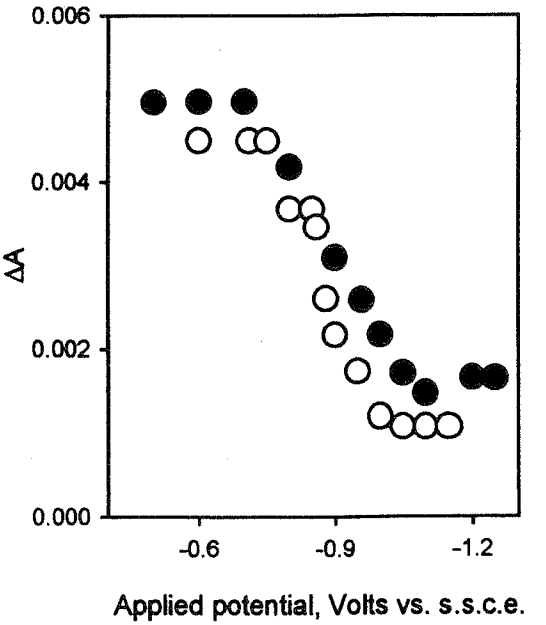

Figure 6. Transient absorbance intensities vs. applied potential for RuL_3^{n-} (filled circles) and OsL_3^{n-} (open circles) on TiO_2 in acetonitrile.

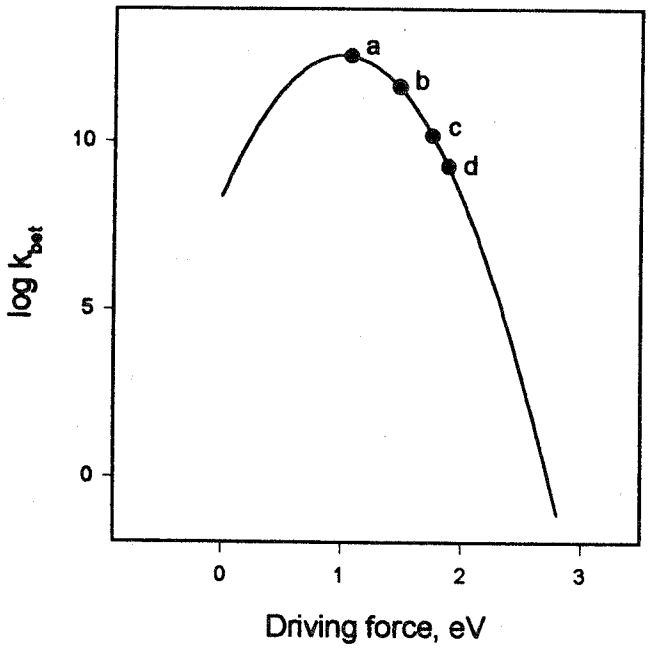

Figure 7. Hypothetical rate vs. driving force curve based on classical Marcus theory with 1 eV reorganization energy. Labeled points correspond to overall reaction driving force for back ET from TiO_2 to: a) OsL_3^{9-} at H_o -4.1, b) OsL_3^{9-} at pH 2.5, c) OsL_3^{9-} at pH 7, and d) RuL_3^{9-} at pH 2.5.